

Disc formation from stellar tidal disruptions

Clément Bonnerot^{1*}, Elena M. Rossi¹, Giuseppe Lodato² and Daniel J. Price³

¹*Leiden Observatory, Leiden University, PO Box 9513, 2300 RA, Leiden, the Netherlands*

²*Dipartimento di Fisica, Università Degli Studi di Milano, Via Celoria, 16, Milano, 20133, Italy*

³*Monash Centre for Astrophysics and School of Mathematical Sciences, Monash University, Clayton, Vic 3800, Australia*

Accepted ?. Received ?; in original form ?

ABSTRACT

The potential of tidal disruption of stars to probe otherwise quiescent supermassive black holes cannot be exploited, if their dynamics is not fully understood. So far, the observational appearance of these events has been commonly derived from analytical extrapolations of the debris dynamical properties just after the stellar disruption. In this paper, we perform hydrodynamical simulations of stars in highly eccentric orbits, that follow the stellar debris *after* disruption and investigate their ultimate fate. We demonstrate that gas debris circularize on an orbital timescale because relativistic apsidal precession causes the stream to self-cross. The higher the eccentricity and/or the deeper the encounter, the faster is the circularization. If the internal energy deposited by shocks during stream self-interaction is readily radiated, the gas forms a narrow ring at the circularization radius. It will then proceed to accrete viscously at a super-Eddington rate, puffing up under radiation pressure. If instead cooling is impeded, the gas forms an extended, mostly centrifugally supported torus. In this case, however, the viscous timescale is comparable to the circularization timescale and the torus is being drained at a super-Eddington rate while forming.

Key words: black hole physics – accretion discs – hydrodynamics – galaxies: nuclei.

1 INTRODUCTION

Most galaxies have been found to contain a supermassive black hole (SMBH) at their centre orbited by stars. If one of these stars wanders too close to the black hole, the tidal force of the black hole exceeds the star’s self-gravity and the star is torn apart. Such an event is called a tidal disruption event (TDE). It occurs when the pericentre distance of the star R_p is smaller than the tidal radius

$$R_t = R_\star \left(\frac{M_h}{M_\star} \right)^{1/3}, \quad (1)$$

where M_h is the mass of the black hole, M_\star and R_\star are the mass and radius of the star (Rees 1988; Lacy, Townes, & Hollenbach 1982). The depth of the encounter is characterized by the penetration factor $\beta = R_t/R_p$. During the disruption, half of the stellar elements experience an increase of their specific orbital energy while the other half undergoes a decrease. This causes the specific orbital energy distribution of the debris to spread around the specific orbital energy ε_\star of the star with a width $\Delta\varepsilon$. These debris then evolve on almost ballistic orbits to form a thin and eccentric stream of gas. If $\varepsilon_\star = 0$, that is if the star is on a parabolic orbit, half of these debris remain bound to

the black hole. This fraction can be larger if $\varepsilon_\star < 0$, that is if the star is on a bound orbit. In particular, if $\varepsilon_\star < -\Delta\varepsilon$, all the debris remain bound to the black hole. This is the case if the eccentricity e of the star satisfies $e < e_{\text{crit}}$ where

$$e_{\text{crit}} = 1 - \frac{2}{\beta} \left(\frac{M_h}{M_\star} \right)^{-1/3} \quad (2)$$

(Hayasaki et al. 2013). The part of the stream composed of bound debris then falls back towards the disruption site. In the standard picture of TDEs, these debris circularize to form an accretion disc. Viscous accretion then drives the emission of a thermal flare from the disc mainly in the UV to soft X-ray band. Handful of candidate TDEs have been detected so far (Gezari et al. 2009, 2012; Komossa 2002; van Velzen et al. 2011).

TDEs are powerful tools to detect SMBHs in otherwise quiescent galaxies. The luminosity detected from these events could in principle be used to put constraints on the properties of both the black hole and the disrupted star. However, deriving such constraints from observations is challenging in practice as it requires a precise understanding of the dynamics of TDEs. Many investigations of these events have been undertaken both analytically and numerically to elucidate the dynamics of tidal disruptions. A distinctive feature of the pioneering works by Lacy et al. (1982); Rees (1988); Evans & Kochanek

* E-mail: bonnerot@strw.leidenuniv.nl

(1989); Phinney (1989) is a $t^{-5/3}$ decrease of the rate at which the stellar debris fall back towards the black hole. This rate was later shown to be dependent on the properties of the star and the black hole (Lodato et al. 2009; Kesden 2012; Guillochon & Ramirez-Ruiz 2013). The same slope is generally fitted to the observed luminosities of TDEs (Esquej et al. 2008; Gezari et al. 2008, 2009; Cappelluti et al. 2009) although it is only expected at late times (Lodato et al. 2009) and in the X-ray band (Lodato & Rossi 2011). This correspondence suggests a fast circularization where the disc forms after only a few orbits of the debris around the SMBH. However, the mechanism driving the circularization is still unknown.

Various effects are likely to be involved in this process whose common feature is to inject a large amount of thermal energy into the newly formed disc. This thermal energy is supplied at the expense of the kinetic energy of the debris whose decrease is at the origin of circularization. However, the efficiency of this energy transfer is certainly dependent on the mechanism considered. The main candidates are the following (Evans & Kochanek 1989; Kochanek 1994):

(i) *Pancake shock*: As the star is disrupted, part of its material is accelerated out of the initial orbital plane. As a result, the debris inside the stream have a range of inclinations. Their orbits are therefore vertically focussed and intersect the orbital plane close to pericentre. At this point, the stream is strongly compressed which causes the formation of a pancake shock.

(ii) *Self-crossing*: When they reach pericentre, the debris experience changes of their apsidal angles driven by relativistic apsidal precession or hydrodynamical effects. This can lead to the self-crossing of the stream: as its leading part moves away from the black hole after its passage at pericentre, it collides with the part that is still falling back. This collision may generate strong shocks.

(iii) *Shearing*: As the stream comes back to pericentre, the orbits of the debris are radially focussed due to their large range of apocentres but small range of pericentres. This effect is similar to a passage into a nozzle. The debris experience shearing at this point as they have a range of apsidal angles and eccentricities induced by the disruption of the star. This effect is enhanced by relativistic apsidal precession: as they have a range of pericentre distances, the orbits of the debris precess by different angles which causes further shearing.

The structure and the evolution of the disc forming from the circularization of the debris are two other uncertainties in the modelisation of TDEs. They depend on the relative efficiency of three processes (Evans & Kochanek 1989): circularization, viscous accretion and radiative cooling. Denoting the timescales of these processes by t_{circ} , t_{visc} and t_{cool} respectively, three limiting regimes are to be expected. In the case $t_{\text{visc}} \ll t_{\text{circ}}$, the debris are drained into the black hole before a disc even forms. In the two other cases, $t_{\text{visc}} \gtrsim t_{\text{circ}}$ which means that a disc forms. If $t_{\text{cool}} \ll t_{\text{circ}}$, this disc cools during its formation and is therefore geometrically thin. If instead $t_{\text{circ}} \ll t_{\text{cool}}$, the disc puffs up while it forms due to its excess of thermal energy. Many authors have assumed that the disc is geometrically thin or slim (Strubbe & Quataert 2009; Cannizzo & Gehrels 2009; Cannizzo et al. 2011;

Lodato & Rossi 2011; Shen & Matzner 2014) using the standard α parametrization (Shakura & Sunyaev 1973). Other investigations considered the possibility of a geometrically thick disc (Loeb & Ulmer 1997; Coughlin & Begelman 2014).

Numerical simulations of tidal disruptions (Evans & Kochanek 1989; Lodato et al. 2009) have often used smoothed particle hydrodynamics (SPH) primarily because of its ability to deal with large regions of space devoid of gas. This technique is also well suited to simulate the subsequent fallback of the debris towards the black hole. The computational cost of such a simulation scales with the total number of SPH particles used to model the stream. To accurately follow their evolution, each part of the stream must contain enough particles. This condition is hard to fulfil for a long stream because the SPH particles are spread on a large volume. The length of the stream increases with the mass ratio $q = M_{\text{h}}/M_{\star}$ and with the eccentricity e of the star. The typical values of these parameters are $q = 10^6$ and $e = 1$. This extreme value of e comes from the fact that most disrupted stars are scattered from distances much larger than R_{t} (Frank & Rees 1976) after a succession of encounters with the other stars surrounding the SMBH. However, as noted by Ayal et al. (2000), following the fallback of the debris for these typical values of q and e numerically is a computational burden. In their simulation, the leading part of the stream is composed of very few SPH particles which come back almost one by one towards the black hole. As a result, the evolution of these particles cannot be followed accurately. Even if they use a relatively low number of particles ($N = 4295$), this issue is so extreme that it is likely to persist for larger particle numbers. The high computational cost of such a simulation is not limited to SPH but generalizes to other computational techniques.

In the few other investigations of this problem, either q or e has therefore been lowered. The first option has been chosen by several authors (Ramirez-Ruiz & Rosswog 2009; Guillochon et al. 2014) who investigated $q = 10^3$ and $e = 1$. The physical motivation in this case is the tidal disruption of a star by an intermediate mass black hole. Both pancake shock and shearing were shown to be inefficient at circularizing the debris in this case. Instead, the main effect seen in these simulations is the expansion of the stream caused by its passage at pericentre. Circularization is more likely driven by self-crossing either induced by this expansion or by relativistic apsidal precession. Hayasaki et al. (2013) made the second choice, as in the present paper, which corresponds to tidal disruptions of bound stars. They considered $q = 10^6$ and $e = 0.8$ and found that self-crossing driven by relativistic precession efficiently drives the circularization of the debris in this case.

Several mechanisms, listed in Hayasaki et al. (2013), are able to put a star on a bound orbit entering the tidal radius of a SMBH. We mention three of them here. The first involves a unequal mass SMBH binary interacting with a surrounding stellar cusp. In this situation, bound stars can be scattered inside the tidal radius of the primary black hole through a combination of Kozai interactions and close encounters with the secondary black hole (Chen et al. 2009, 2011). The second mechanism takes place during the coalescence of a SMBH binary. Due to the anisotropic emission of gravitational waves in this phase, the remnant black

hole undergoes a kick. It can lead to close encounters between the black hole and the surrounding stars leading to their tidal disruptions (Stone & Loeb 2011). Furthermore, mean-motion resonances can pull surrounding stars inwards during the final phase of the SMBH merger (Seto & Muto 2010) enhancing the rate of tidal disruptions of bound stars by this mechanism. The third mechanism takes place after the tidal separation of a stellar binary by a black hole which places the components on an eccentric orbit. Due to both encounters with the other stars orbiting the SMBH and gravitational wave emission, its orbit shrinks and circularize. Under certain conditions, it can then be tidally disrupted by the SMBH on a bound orbit (Amaro-Seoane et al. 2012).

Using SPH simulations, we investigate in this paper the circularization process leading to the formation of the disc. We also characterize the structure and evolution of this disc. Relativistic apsidal precession, involved in the circularization process, is treated exactly while most previous studies (Ramirez-Ruiz & Rosswog 2009; Guillochon et al. 2014; Hayasaki et al. 2013) used an approximate treatment of this effect. In addition, the circularization of the debris is analysed through a careful examination of their orbital energy distribution. The parameters that are likely to play a significant role in the circularization process have also been varied. Two extreme cooling efficiencies, encoded in the equation of state (EOS) of the gas, have been considered. The effect of the orbit of the star has also been examined, by varying both its penetration factor and its eccentricity. Our results demonstrate that circularization is a fast process, happening in a few orbits of the debris around the black hole, and driven mostly by relativistic apsidal precession. They also confirm the expected effect of the cooling efficiency on the structure of the resulting disc. In addition, we found different channels of circularization for different orbits of the star. In particular, by increasing its eccentricity, we got insight into the circularization process at work in the standard parabolic case.

This paper is organized as follows. In Section 2, we describe the SPH simulations performed. The results of these simulations are presented in Section 3 varying the following parameters: the gravitational potential, the EOS, the penetration factor and the eccentricity of the star. The effect of the resolution on these results is also examined. In Section 4, we discuss these results and make predictions on the subsequent evolution of the disc.

2 SPH SIMULATIONS

We investigate the tidal disruption of a star of mass $M_* = 1 M_\odot$ and radius $R_* = 1 R_\odot$ by a non-rotating black hole of mass $M_h = 10^6 M_\odot$. Several initial elliptical orbits of the star are considered. They have different penetration factors $\beta = 1$ and $\beta = 5$ corresponding to pericentre distances $R_p = 100 R_\odot$ and $R_p = 20 R_\odot$ respectively. For $\beta = 1$, only an eccentricity $e = 0.8$ is considered. For $\beta = 5$, two different values $e = 0.8$ and $e = 0.95$ are investigated. All these orbits satisfy the condition $e < e_{\text{crit}}$ where e_{crit} is given by (2). It implies that all the debris produced by the disruption stay bound to the black hole. The semi-major axis $a_* = R_p/(1 - e)$ of these orbits range between

- SPH simulation
- - Relativistic potential
- ... Schwarzschild metric

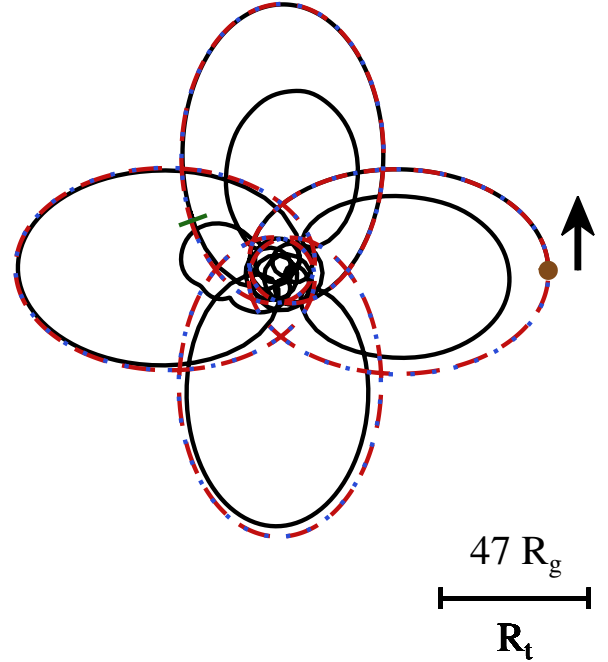


Figure 1. Trajectory of the centre of mass of the gas in the simulation corresponding to model RI5e.8 (black solid line) compared to that of a test particle on the same orbit in the relativistic potential (red dashed line) and in the Schwarzschild metric (blue dotted line). All the trajectories start at the initial position of the star indicated by the brown point on the right of the figure. The black arrow specifies the direction of motion. The trajectory of the test particle in the relativistic potential and in the Schwarzschild metric is followed for 4 orbits. That of the centre of mass of the gas in the simulation is followed during the disruption of the star and the fallback of the debris until $t/P_* = 8$. The transition between the disruption and the fallback phase, treated with two different codes, is indicated by the green dash perpendicular to this trajectory. After a few pericentre passages, the motion of the gas is affected by hydrodynamical effects and the trajectory of its centre of mass differs from that of a test particle.

$100 R_\odot$ and $500 R_\odot$ which corresponds to orbital periods $P_* = 2\pi (GM_h/a_*^3)^{-1/2}$ between 2.8 h and 31 h.

Both the disruption of the star and the subsequent fallback of the debris towards the disruption site are simulated using SPH. To increase efficiency, the simulations of these two phases are performed separately and make use of two different codes, each adapted to a specific phase. For the disruption phase, we use a code which takes into account self-gravity (Bate et al. 1995). For the fallback phase, we do not consider self-gravity and make use of the highly efficient code PHANTOM (Price & Federrath 2010; Lodato & Price 2010) which is optimized for studying non-self-gravitating

problems¹. This choice is legitimate because the self-gravity force is only needed during the disruption phase where it opposes the tidal force of the black hole. In the fallback phase, the gravitational interactions between the debris is negligible compared to their hydrodynamical interactions and the tidal interactions with the black hole. The disruption phase is followed until the most bound debris come back to pericentre. Their properties are recorded at this point and constitute the initial conditions for the simulation of the fallback phase. As this paper's primary focus is on the fallback of the debris, the disruption phase is only simulated to get these initial conditions and not discussed in detail.

The code used for the disruption phase has already been adopted by Lodato et al. (2009) to simulate tidal disruptions of stars on parabolic orbits. In the present paper, we follow the same procedure and numerical setup but consider elliptical orbits instead. Also using the same method, we model the star as a polytropic sphere with $\gamma = 5/3$ containing 100K particles. However, as explained in subsection 3.4, the fallback phase is simulated at a higher resolution with the stream of debris containing 500K particles.

In order to resolve the shocks, the code used for the fallback phase, PHANTOM, includes the standard artificial viscosity prescription which depends on the parameters α^{AV} and β^{AV} . In addition, the Morris & Monaghan (1997) switch is implemented which aims at reducing artificial dissipation away from shocks. To this end, α^{AV} is allowed to vary between two extremal values α_{\min}^{AV} and α_{\max}^{AV} according to a source and decay equation. In this paper, we use $\alpha_{\min}^{AV} = 0.01$, $\alpha_{\max}^{AV} = 1$ and $\beta^{AV} = 2$.

The orbits considered for the star have pericentre distances comparable with the gravitational radius $R_g = GM_h/c^2$ of the black hole. More precisely, $R_p = 47R_g$ and $R_p = 9.4R_g$ for $\beta = 1$ and $\beta = 5$. Therefore, relativistic effects must significantly affect the motion of the gas when it passes at pericentre. One of these effects is relativistic apsidal precession, a mechanism involved in the circularization process. It causes the orbit of a test particle to precess at each pericentre passage by a given precession angle. For the orbits considered, the precession angle varies between 13.5 and 89.7 degrees for $\beta = 1$ and $\beta = 5$ respectively. In order to investigate the influence of relativistic effects, the black hole is modelled by an external potential which is either Keplerian or relativistic both in the disruption and the fallback phase. In the following, the variables are labelled by the letter K if they are computed in the Keplerian potential and by the letter R if they are computed in the relativistic potential. These potentials are respectively given by

$$\Phi^K = -\frac{GM_h}{R}, \quad (3)$$

$$\Phi^R = -\frac{GM_h}{R} - \left(\frac{2R_g}{R-2R_g}\right) \left[\left(\frac{R-R_g}{R-2R_g}\right) v_r^2 + \frac{v_t^2}{2} \right], \quad (4)$$

where v_r and v_t are respectively the radial and tangential velocity of a test particle. We adopt this relativistic potential, designed by Tejeda & Rosswog (2013), because it contains an exact treatment of apsidal precession around a non-rotating black hole. In other words, the value of the

precession angle for a test particle on a given orbit is the same in this potential and in the Schwarzschild metric. It is an improvement compared to most previous investigations which used an approximate treatment of this effect (Ramirez-Ruiz & Rosswog 2009; Guillochon et al. 2014; Hayasaki et al. 2013).

For the disruption phase, the star is initially placed at the apocentre of its orbit, a distance $R_a = (1+e)R_p/(1-e)$ from the black hole. Its initial velocity v_a is determined by conservation of specific orbital energy and angular momentum between R_a and R_p . In the Keplerian and relativistic potentials, the specific orbital energy is respectively given by

$$\varepsilon^K = \frac{1}{2} (v_r^2 + v_t^2) - \frac{GM_h}{R}, \quad (5)$$

$$\varepsilon^R = \frac{1}{2} \left[\left(\frac{R}{R-2R_g}\right)^2 v_r^2 + \left(\frac{R}{R-2R_g}\right) v_t^2 \right] - \frac{GM_h}{R}, \quad (6)$$

and the specific angular momentum by

$$l^K = Rv_t, \quad (7)$$

$$l^R = \frac{Rv_t}{R-2R_g}. \quad (8)$$

The initial velocity of the star at apocentre is therefore

$$v_a^K = \left(\frac{GM_h}{R_a}\right)^{1/2} \left(\frac{2R_p}{R_a+R_p}\right)^{1/2} \quad (9)$$

$$= \left(\frac{GM_h}{R_a}\right)^{1/2} (1-e)^{1/2}, \quad (10)$$

$$v_a^R = \left(\frac{GM_h}{R_a}\right)^{1/2} \frac{2^{1/2}R_p(R_a-2R_g)}{R_a((R_a+R_p)(R_p-2R_g)+2R_gR_p^2)^{1/2}}, \quad (11)$$

depending on the potential.

In order to demonstrate the correct implementation of the relativistic potential into the SPH codes, we anticipate the next section and analyse the motion of the gas in the simulation associated to model RI5e.8. In this model, the relativistic potential is used and the orbit of the star has a penetration factor $\beta = 5$ and an eccentricity $e = 0.8$. Fig. 1 shows the trajectory of the centre of mass of the gas in the simulation corresponding to model RI5e.8 compared to that of a test particle on the same orbit in the relativistic potential and in the Schwarzschild metric. The trajectory of the test particle in the relativistic potential and in the Schwarzschild metric is followed for 4 orbits. That of the centre of mass of the gas is followed during both the disruption of the star and the fallback of the debris until $t/P_\star = 8$. The trajectory of the test particle is the same in the relativistic potential and in the Schwarzschild metric. It confirms that apsidal precession is treated accurately in the relativistic potential as found by Tejeda & Rosswog (2013). During the disruption and the beginning of the fallback phase, the centre of mass of the gas and the test particle have the same trajectory. It validates the implementation of the potential into the SPH codes. After a few pericentre passages, the two trajectories start to differ as the hydrodynamical effects on the debris become dominant. This evolution will be investigated in detail in the next section.

The accretion onto the black hole is modelled by an accretion radius fixed at the innermost stable circular orbit,

¹ Self-gravity is now implemented into PHANTOM. However, it was not available at the beginning of this work.

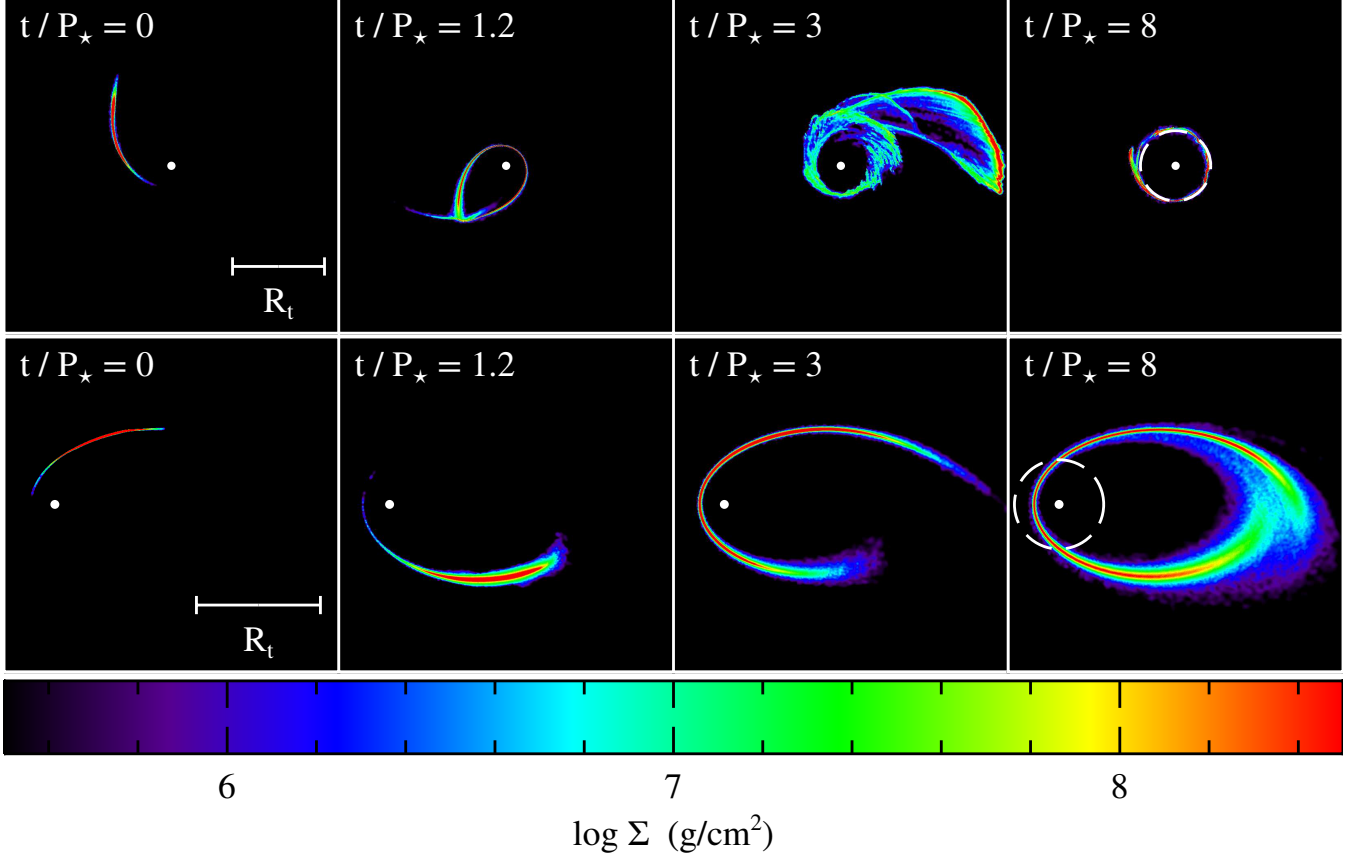


Figure 2. Snapshots of the fallback of the debris at different times $t/P_\star = 0, 1.2, 3$ and 8 for models RI5e.8 (upper panel) and KI5e.8 (lower panel). For these models, the period of the star P_\star is 2.8 h. The colours correspond to the column density Σ of the gas whose value is indicated on the colour bar. The white point represents the black hole. The dashed white circle on the last snapshot represents the circularization radius given by equations (14) and (15) for the Keplerian and relativistic potentials respectively.

Table 1. Name and parameters of the different models.

Model	Potential	EOS	β	e
RI5e.8	Relativistic	Locally isothermal	5	0.8
KI5e.8	Keplerian	Locally isothermal	5	0.8
RA5e.8	Relativistic	Adiabatic	5	0.8
KA5e.8	Keplerian	Adiabatic	5	0.8
RI1e.8	Relativistic	Locally isothermal	1	0.8
RA1e.8	Relativistic	Adiabatic	1	0.8
RI5e.95	Relativistic	Locally isothermal	5	0.95
RA5e.95	Relativistic	Adiabatic	5	0.95

of $6R_g$ for a non-rotating black hole. Particles entering this radius are removed from the simulations.

The simulation of the fallback phase is performed for two different equations of state (EOS) for the gas: locally isothermal and adiabatic. For the locally isothermal EOS, each debris, or SPH particle, keep their initial specific thermal energies. Physically, these two EOS represent the two extreme cases for the rate at which an excess of thermal energy is radiated away from the gas. For the locally isothermal one, every increase of thermal energy is instantaneously radiated away while for the adiabatic one, none of this energy is radiated.

Four parameters are therefore considered to simulate

the fallback of the debris: the potential, the EOS, the penetration factor β and the eccentricity e . The values of these parameters for the eight models investigated in this paper are shown in table 1.

3 RESULTS

In this section, we present the results of the simulations of the fallback phase². The starting point of these simulations, corresponding to $t = 0$, is when the most bound debris of the stream come back to pericentre. The circularization process is investigated through the evolution of both the position and the specific orbital energy of the debris. They will be respectively compared to the so called circularization radius and specific circularization energy.

These two quantities are defined as follows. Before the disruption, the distribution of specific angular momentum of the gas inside the star is sharply peaked around the specific angular momentum of the star. This distribution is not significantly affected by the disruption. Therefore, at the beginning of the fallback phase, the debris inside the stream

² Movies of the simulations presented in this paper are available at <http://home.strw.leidenuniv.nl/~bonnerot/research.html>.

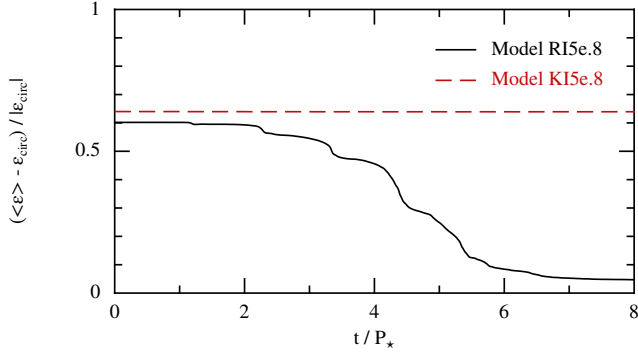


Figure 3. Evolution of the average specific orbital energy of the debris for models RI5e.8 and KI5e.8. For these models, the period of the star P_\star is 2.8 h. The average specific orbital energy is shown relative to the specific circularization energy given by equations (16) and (17) for the Keplerian and relativistic potentials respectively.

still have specific angular momenta close to that of the star. If the debris then move from their initial eccentric orbits to circular orbits each of them conserving their individual specific angular momentum, these circular orbits form at similar radii. They are located at a distance from the black hole called the circularization radius. This radius is determined by equating the specific angular momentum of the star, given by equations (7) and (8) evaluated at apocentre, and the specific circular angular momentum given by

$$l_c^K = (GM_h R)^{1/2}, \quad (12)$$

$$l_c^R = \frac{(GM_h)^{1/2} R}{(R - 3R_g)^{1/2}}, \quad (13)$$

in the Keplerian and relativistic potentials respectively. It yields a circularization radius of

$$R_{\text{circ}}^K = \frac{R_a^2 v_a^2}{GM_h} = (1 + e) R_p, \quad (14)$$

$$R_{\text{circ}}^R = \frac{R_a^4 v_a^2 + (R_a^4 v_a^2 (-12GM_h (R_a - 2R_g)^2 R_g + R_a^4 v_a^2))^{1/2}}{2GM_h (R_a - 2R_g)^2}, \quad (15)$$

where v_a is given by equations (9) or (11) depending on the potential. The associated specific orbital energy is called specific circularization energy. It is equal to the specific circular orbital energy evaluated at the circularization radius. In the two potentials, the specific circularization energy is

$$\epsilon_{\text{circ}}^K = -\frac{GM_h}{2R_{\text{circ}}} = -\frac{GM_h}{2(1+e)R_p}, \quad (16)$$

$$\epsilon_{\text{circ}}^R = -\frac{GM_h}{2R_{\text{circ}}} \left(\frac{R_{\text{circ}} - 4R_g}{R_{\text{circ}} - 3R_g} \right), \quad (17)$$

where R_{circ} is given by equations (14) or (15) depending on the potential.

3.1 Impact of relativistic precession

We start by analysing the impact of relativistic precession on the fallback of the debris. Among all the orbits considered, this effect is the strongest for a star with a penetration factor $\beta = 5$ and an eccentricity $e = 0.8$. This is because it has the lowest pericentre distance $R_p = 9.4R_g$ and, to a smaller

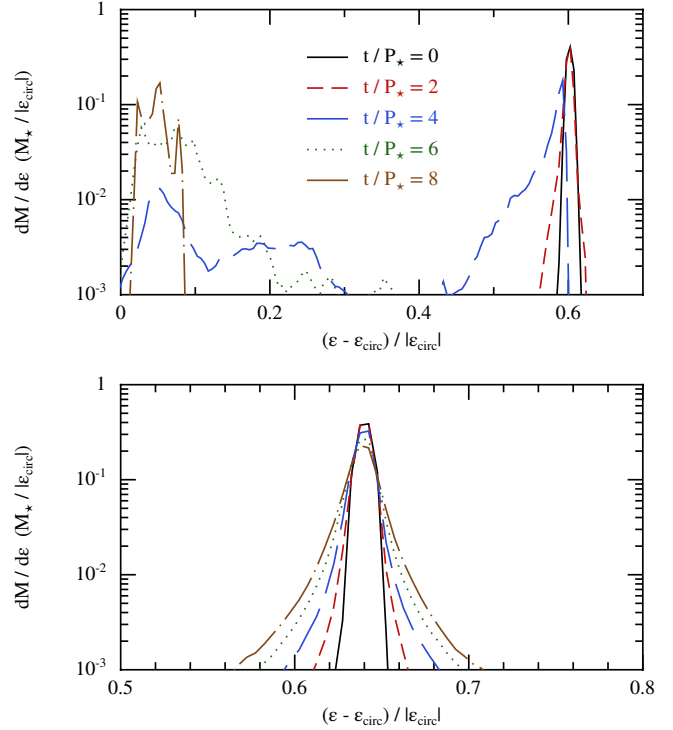


Figure 4. Specific orbital energy distributions of the debris at different times $t/P_\star = 0, 2, 4, 6$ and 8 for model RI5e.8 (upper panel) and KI5e.8 (lower panel). For these models, the period of the star P_\star is 2.8 h. The specific orbital energy is shown relative to the specific circularization energy given by equations (16) and (17) for the Keplerian and relativistic potentials respectively.

extent, the lowest eccentricity. In this case, the precession angle is 89.7 degrees. We investigate the role of relativistic precession for a star on this orbit by comparing models RI5e.8 and KI5e.8. In model RI5e.8, the relativistic potential is used and apsidal precession is taken into account. In model KI5e.8, the potential used is Keplerian and apsidal precession is not considered. In each potential, the orbit of the star has fixed pericentre and apocentre distances, the latter being obtained from the former via the eccentricity. The initial velocity of the star is different in the Keplerian and relativistic potentials and given by equations (9) and (11) respectively. In both models, a locally isothermal EOS is adopted for the gas.

We discuss model RI5e.8 first. Fig. 2 (upper panel) shows snapshots of the fallback of the debris at different times $t/P_\star = 0, 1.2, 3$ and 8. Fig. 3 (black solid line) and Fig. 4 (upper panel) respectively show the evolution of the average specific orbital energy of the debris and their specific orbital energy distributions at different times $t/P_\star = 0, 2, 4, 6$ and 8. The most bound debris of the stream produced by the disruption of the star reaches pericentre at $t/P_\star = 0$. The stream self-crosses due to apsidal precession at $t/P_\star \simeq 1.2$ that is after the second pericentre passage of its leading part (Fig. 2). As a result, it undergoes shocks that convert kinetic energy into thermal energy. A crucial point is that the EOS used is locally isothermal. It corresponds to a situation where the excess thermal energy is instantaneously radiated away from the debris. Therefore, the net effect of these shocks is to remove kinetic energy from the

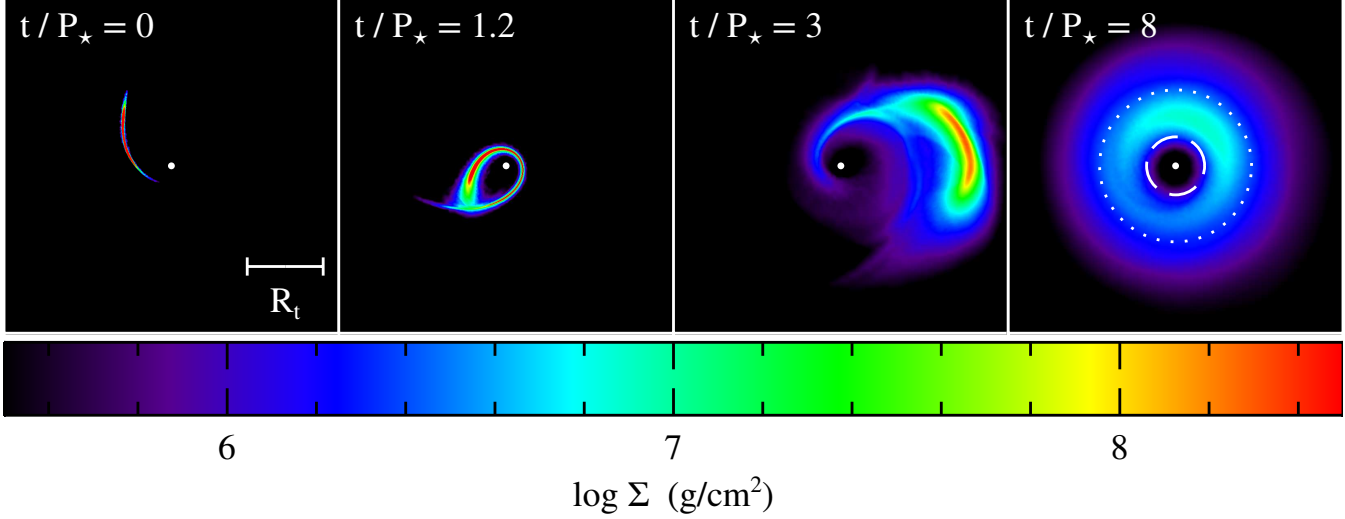


Figure 5. Snapshots of the fallback of the debris at different times t/P_* = 0, 1.2, 3 and 8 for model RA5e.8. For this model, the period of the star P_* is 2.8 h. The colours correspond to the column density Σ of the gas whose value is indicated on the colour bar. The white point represents the black hole. The dashed white circle on the last snapshot represents the circularization radius given by equation (15) for the relativistic potential. The dotted white circle represents the semi-major axis of the star.

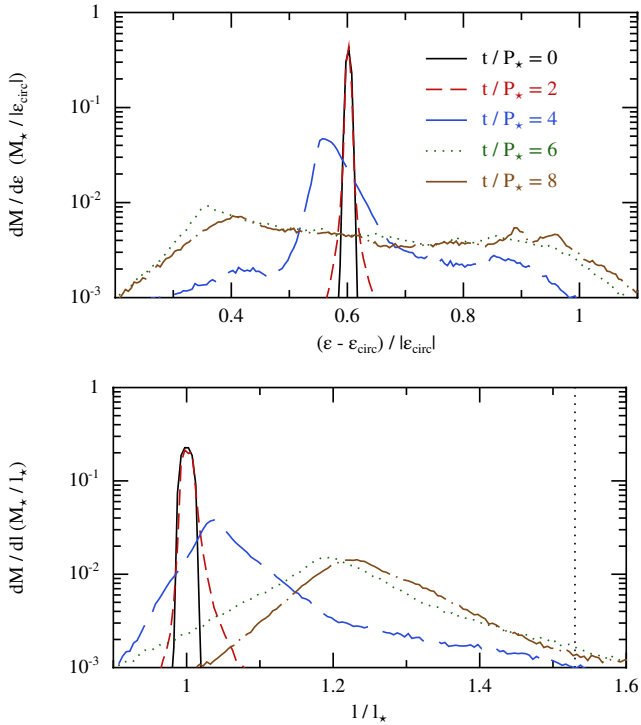


Figure 6. Specific orbital energy distribution (upper panel) and specific angular momentum distribution (lower panel) of the debris at different times t/P_* = 0, 2, 4, 6 and 8 for model RA5e.8. For this model, the period of the star P_* is 2.8 h. The specific orbital energy is shown relative to the specific circularization energy given by equation (17) for the relativistic potential. The specific angular momentum is shown relative to that of the star given by equation (13) evaluated at apocentre.

stream. As a consequence, the average specific orbital energy of the debris starts to decrease at this time (Fig. 3). Self-crossings occur after each pericentre passage of the leading part of the stream. Each of them generate shocks which re-

move more kinetic energy from the debris. As a consequence, their average specific orbital energy continues to decrease for $t/P_* \gtrsim 1.2$ (Fig. 3). This decrease presents periodic steeper phases which coincide with the self-crossings of the stream. Accordingly, the specific orbital energy distribution of the debris shifts towards lower energies (Fig. 4). As a result, the debris progressively move to circular orbits. For example, at $t/P_* = 3$, a small fraction of the debris is on circular orbits while the majority of them are still on eccentric orbits (Fig. 2). At $t/P_* \simeq 8$, the average specific orbital energy of the debris settles at a value comparable but somewhat larger than the specific circularization energy (Fig. 3). Accordingly, their distribution of specific orbital energy stabilizes around this value (Fig. 4). At this time, the debris settle into a thin and narrow ring of radius similar to the circularization radius but slightly larger (Fig. 2).

These small discrepancies with the specific circularization energy and the circularization radius are due to redistribution of angular momentum between the debris during the shocks occurring when the stream self-crosses. Part of the debris experience a decrease of their specific angular momentum which leads to the accretion of some of them onto the black hole. This causes an excess of angular momentum which is redistributed among the remaining debris. As a result, they all undergo an increase of their specific angular momentum. Therefore, they form circular orbits at radii larger than the circularization radius. This is because the latter has been computed by assuming that each of the debris keeps their individual specific angular momentum while moving to circular orbits. As a consequence, their specific orbital energy is also larger than the specific circularization energy. These discrepancies are suppressed when the resolution of the simulations is increased as will be shown in subsection 3.4.

We now discuss model KI5e.8 for which the evolution of the debris is very different. Fig. 2 (lower panel) shows snapshots of the fallback of the debris at different times $t/P_* = 0, 1.2, 3$ and 8. The evolution of the average specific

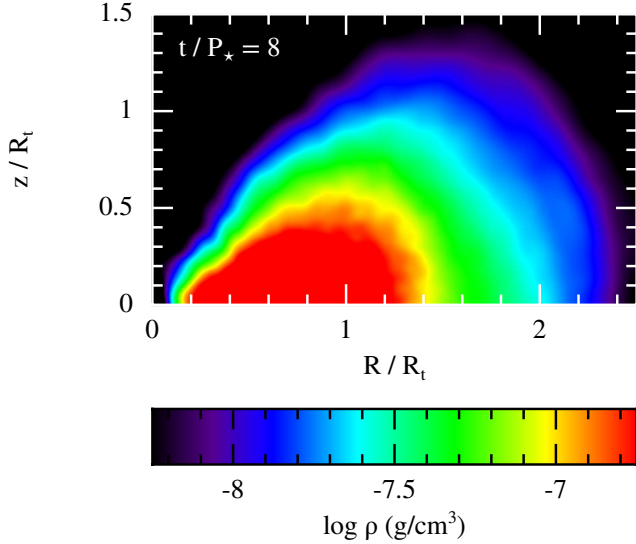


Figure 7. Cross-section in the $R-z$ plane of the torus formed at $t/P_* = 8$ for model RA5e.8. z represents the height with respect to the midplane and R the cylindrical radius. The distances are normalized by the tidal radius given by equation (1). The black hole is at the origin. The colours correspond to the density ρ of the gas whose value is indicated on the colour bar.

orbital energy of the debris is shown in Fig. 3 (red dashed line) and their specific orbital energy distributions at different times $t/P_* = 0, 2, 4, 6$ and 8 are shown in Fig. 4 (lower panel). As there is no apsidal precession, the stream does not self-cross (Fig. 2). Therefore, it does not undergo shocks and no kinetic energy is removed from the debris. Accordingly, the specific orbital energy of the debris remains constant (Fig. 3) and their specific orbital energy distribution stays peaked around its initial value. It also spreads somewhat due to tidal effects (Fig. 4). As a result, the debris do not move to circular orbits and settle instead at $t/P_* \simeq 8$ into an elliptical structure centred around the initial orbit of the star and outside the circularization radius (Fig. 2).

The comparison of models RI5e.8 and KI5e.8 shows the fundamental role of apsidal precession in the circularization process.

3.2 Influence of the cooling efficiency

We now investigate the effect of the cooling efficiency. In the previous subsection, the evolution of the debris has been analysed for models RI5e.8 and KI5e.8. For these models, a locally isothermal EOS is used. It corresponds to a very efficient cooling where every increase of the thermal energy of the debris is instantaneously radiated away. In this subsection, we discuss models RA5e.8 and KA5e.8 that use an adiabatic EOS for the gas instead. It corresponds to a very inefficient cooling where none of the excess thermal energy is radiated away. The potential used is relativistic for model RA5e.8 and Keplerian for model KA5e.8. The star is on the same orbit as for models RI5e.8 and KI5e.8 with a penetration factor $\beta = 5$ and an eccentricity $e = 0.8$.

We discuss model RA5e.8 first. Fig. 5 shows snapshots of the fallback of the debris at different times $t/P_* = 0, 1.2, 3$ and 8 . Fig. 6 shows the specific orbital energy distribution

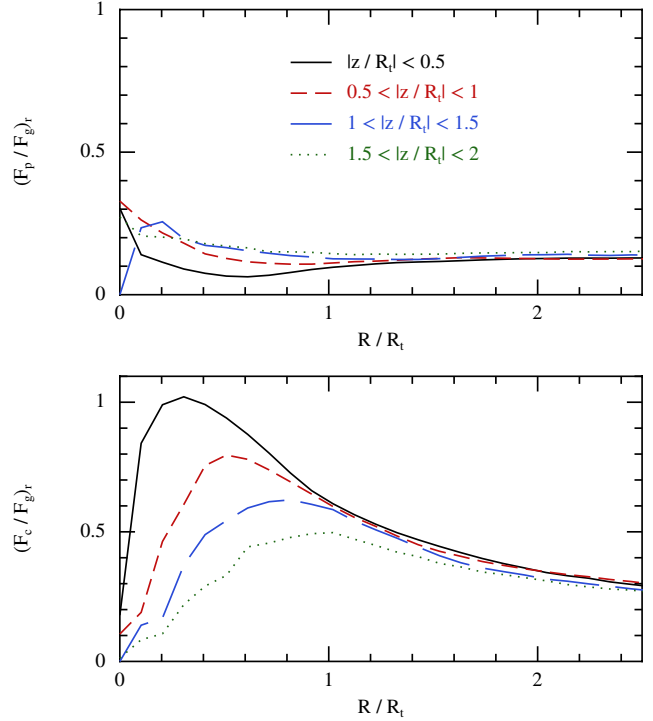


Figure 8. Azimuthally-averaged ratios of the pressure (upper panel) and centrifugal (lower panel) forces to the gravitational force projected in the spherical radial direction as a function of the cylindrical radius R at $t/P_* = 8$ for model RA5e.8. These ratios are shown for different heights z with respect to the midplane: $|z/R_t| < 0.5$, $0.5 < |z/R_t| < 1$, $1 < |z/R_t| < 1.5$ and $1.5 < |z/R_t| < 2$. The distances are normalized by the tidal radius given by equation (1).

(upper panel) and specific angular momentum distribution (lower panel) of the debris at different times $t/P_* = 0, 2, 4, 6$ and 8 . The stream self-crosses at $t/P_* \simeq 1.2$ (Fig. 5). As a result, it experiences shocks which convert kinetic energy into thermal energy. This early evolution is similar to model RI5e.8. However, the subsequent behaviour differs. For model RI5e.8, the only effect of the shocks is to remove kinetic energy from the stream as the excess thermal energy is instantaneously radiated away. However, for model RA5e.8, the thermal energy produced by the shocks is not radiated but kept in the stream. As more self-crossings occur, more thermal energy is injected into the debris. As a result, the stream expands for $t \gtrsim 1.2$ under the influence of thermal pressure (Fig. 5). During this expansion, thermal energy is transferred back into kinetic energy. Kinetic energy is therefore not removed from the debris and their average specific orbital energy is conserved. Instead, the expansion causes the debris to move on a wider range of orbits, either closer or further from the black hole, by redistributing orbital energy between them. Accordingly, their specific orbital energy distribution gets spread (Fig. 6). During the expansion, the ordered motion of the stream is also suppressed and the debris depart from their initial eccentric orbits. This process is accompanied by a redistribution of specific angular momentum between the debris. The distribution of specific angular momentum of the debris gets spread while its peak shifts to slightly larger angular momenta (Fig. 6). It also presents a tail at large angular momenta which reaches

at $t/P_\star \simeq 8$ the specific circular angular momentum at the semi-major axis of the star. The latter is shown on the lower panel of Fig. 6 by a vertical black dotted line. Accordingly, the debris settle into a thick and extended torus in which most of the debris are located at a distance from the black hole outside the circularization radius but inside the semi-major axis of the star (Fig. 5). At this time, most of the debris (91%) are still bound to the black hole (Fig. 6).

Besides getting spread, the specific angular momentum distribution of the debris as a whole shifts to larger angular momenta. As for model RI5e.8, this is due to redistribution of angular momentum between the debris during the shocks.

A more precise analysis of the torus formed at $t/P_\star = 8$ can be done by examining its internal configuration. Fig. 7 shows a cross-section in the $R - z$ plane where z represents the height with respect to the midplane and R the cylindrical radius. It exhibits funnels around the rotation axis. It also contains a dense inner region at $z/R_t \lesssim 0.5$ and $R/R_t \simeq 1$, which corresponds to the semi-major axis of the star. This dense region is surrounded by a more diffuse one which extends from close to the black hole to $R/R_t \simeq 2.5$ and $z/R_t \simeq 1.5$. In addition, we investigate the balance between the different forces in this torus. The only inward force is the gravitational force F_g which is obtained from the relativistic potential. The two outward forces involved are the centrifugal force F_c and the pressure force F_p . Fig. 8 shows azimuthally-averaged ratios of the pressure force (upper panel) and centrifugal force (lower panel) to the gravitational force projected in the spherical radial direction as a function of R and for different intervals of z : $|z/R_t| < 0.5$, $0.5 < |z/R_t| < 1$, $1 < |z/R_t| < 1.5$ and $1.5 < |z/R_t| < 2$. The ratio of the pressure force to the gravitational force is roughly $(F_p/F_g)_r \simeq 0.2$ in the entire torus implying that it is not hydrostatically supported. This is because the thermal energy has been transferred into kinetic energy during the expansion. However, the ratio of the centrifugal force to the gravitational force is larger. For $|z/R_t| < 0.5$, it presents a maximum of $(F_c/F_g)_r \simeq 1$ at $R/R_t \simeq 0.3$ and decreases at larger radii. The same dependence exists for regions further from the midplane but for lower maxima of $(F_c/F_g)_r \simeq 0.5 - 0.8$. Therefore, this torus is mostly centrifugally supported against gravity with this support being stronger in its inner region. As they are bound to the black hole, the regions that are not supported against gravity will stop expanding and collapse at a later time.

For model KA5e.8, the stream expands when it passes at pericentre. Even if relativistic apsidal precession is not present, this expansion causes the stream to self-cross which happens first at $t/P_\star \simeq 4$ that is after the fifth passage of its leading part at pericentre. The subsequent evolution is similar to model RA5e.8. The debris settle into a thick and extended torus at $t/P_\star \simeq 10$. Therefore, relativistic apsidal precession is not necessary for the debris to move to circular orbits. However, it needs to be considered for a realistic description of the motion of the gas.

3.3 Dependence on the orbit of the star

So far, the fallback of the debris has been investigated for a fixed orbit of the star with a penetration factor $\beta = 5$ and an eccentricity $e = 0.8$. We now analyse the effect of

varying the orbit of the star. Two new orbits are considered. They are obtained from the initial orbit by decreasing the penetration factor and increasing the eccentricity.

3.3.1 Decreasing the penetration factor

We start by investigating the effect of decreasing the penetration factor from $\beta = 5$ for the initial orbit to $\beta = 1$ keeping the eccentricity to its initial value $e = 0.8$. This decrease of the penetration factor corresponds to an increase of the associated pericentre distance from $R_p = 9.4R_g$ to $R_p = 47R_g$. Therefore, relativistic precession is weaker. The precession angle decreases from 89.7 for $\beta = 5$ to 13.5 degrees for $\beta = 1$. We investigate the fallback of the debris for a star on this new orbit by discussing models RI1e.8 and RA1e.8. A locally isothermal EOS is used for model RI1e.8 while an adiabatic EOS is used for model RA1e.8. The relativistic potential is used in both models. The corresponding models for the initial orbit, models RI5e.8 and RA5e.8, will be used as references.

We discuss model RI1e.8 first. Fig. 9 shows snapshots of the fallback of the debris at different times $t/P_\star = 0, 2.2, 4, 6, 8$ and 16. Fig. 10 (red dashed line) shows the evolution of the average specific orbital energy of the debris. It also shows this evolution for model RI5e.8 (black solid line). The stream first self-crosses at $t/P_\star = 2.2$ after the third pericentre passage of its leading part due to relativistic precession (Fig. 9). It causes the formation of shocks. As a locally isothermal EOS is used, the thermal energy is instantaneously radiated away from the debris and the net effect of these shocks is to remove kinetic energy from the stream. As a result, the average specific orbital energy of the debris starts to decrease at this time (Fig. 10). It keeps decreasing for $t/P_\star \gtrsim 2.2$ as self-crossings happen after each pericentre passage of the leading part of the stream. However, as relativistic precession is weaker for model RI1e.8 than for model RI5e.8, these shocks are less efficient at removing kinetic energy from the debris. Therefore, this decrease is slower and more gradual. Accordingly, the debris move from their initial eccentric orbits to circular orbits more slowly and as a whole (Fig. 9). This behaviour is different from model RI5e.8 where each self-crossing causes individual parts of the stream to move to circular orbits. At $t/P_\star \simeq 16$, the average specific orbital energy of the debris stabilizes at a value similar but somewhat larger than the circularization energy (Fig. 10). Accordingly, the debris settle into a thin and narrow ring of radius comparable to the circularization radius but somewhat larger (Fig. 9). As for model RI5e.8, the origin of these small discrepancies with the specific circularization energy and the circularization radius is redistribution of angular momentum between the debris.

For model RA1e.8, the evolution of the debris is very similar to model RA5.8. The shocks produced by the self-crossings of the stream leads to the expansion of the debris which settle into a thick and extended torus. In this torus, most of the debris are located between the circularization radius and the semi-major axis of the star. The only effect of modifying the orbit is to change the value of these two limiting radii.

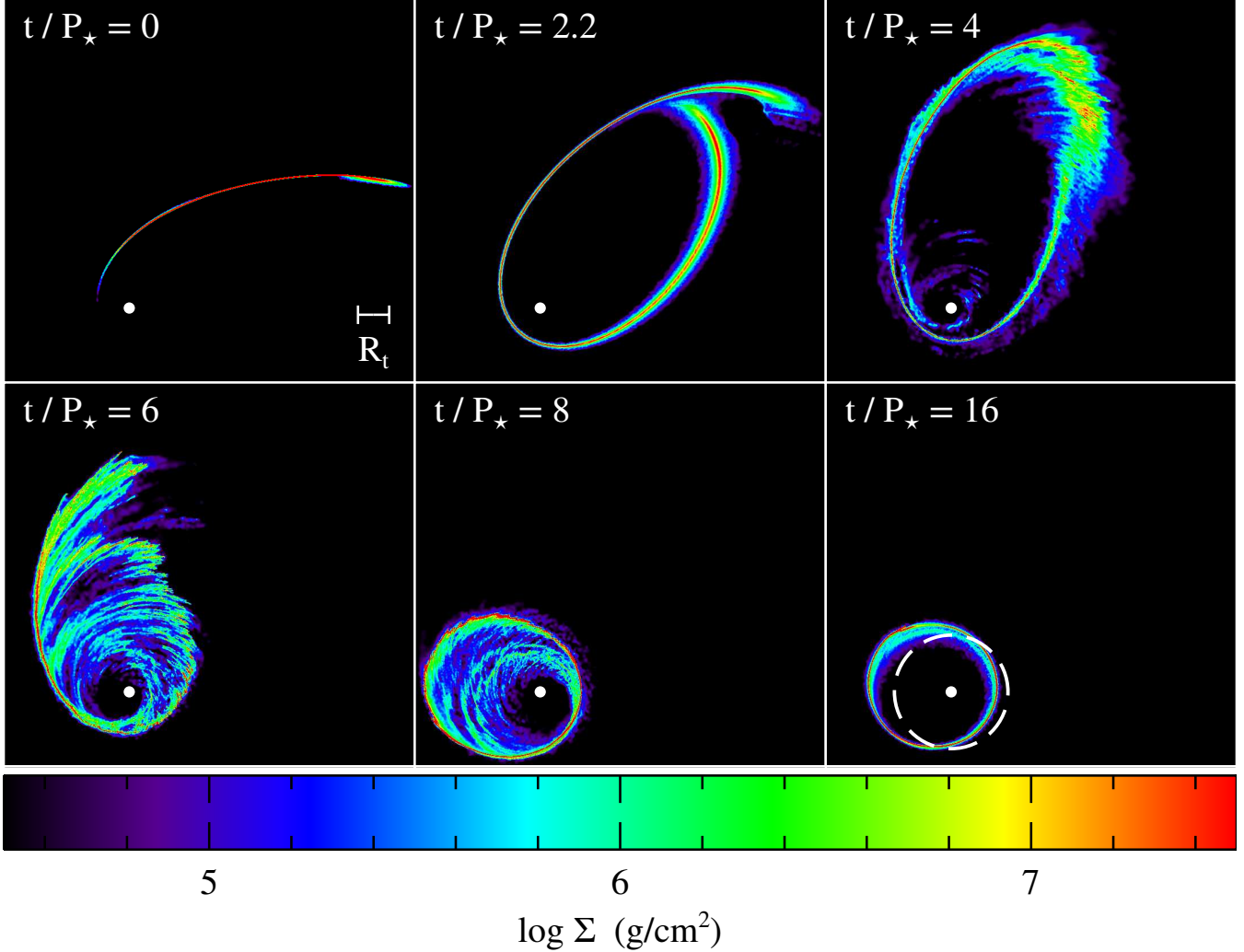


Figure 9. Snapshots of the fallback of the debris at different times $t/P_\star = 0, 2.2, 4, 6, 8$ and 16 for models RI1e.8. For this model, the period of the star P_\star is 31 h. The colours correspond to the column density Σ of the gas whose value is indicated on the colour bar. The white point represents the black hole. The dashed white circle on the last snapshot represents the circularization radius given by equation (15) for the relativistic potential. Apsidal precession is weaker for this model than for model RI5e.8 as the pericentre distance is larger. As a result, the debris move slower to circular orbits due to the self-crossings of the stream.

3.3.2 Increasing the eccentricity

We now evaluate the effect of increasing the eccentricity. The new orbit has an eccentricity $e = 0.95$ while it was $e = 0.8$ for the initial orbit. The penetration factor is kept to its initial value $\beta = 5$. This strength of relativistic precession is not significantly affected by the increase of eccentricity. The precession angle only decreases from 89.7 degrees for $e = 0.8$ to 80.7 degrees for $e = 0.95$. The main difference is that the stream is longer for $e = 0.95$ than for $e = 0.8$. The fallback of the debris is investigated for this new orbit by discussing models RI5e.95 and RA5e.95. For these two models, a locally isothermal and an adiabatic EOS are used respectively. The relativistic potential is considered for both of them. As previously, the corresponding models, RI5e.8 and RA5e.8, are mentioned for comparison.

We discuss first model RI5e.95. Fig. 11 shows snapshots of the fallback of the debris at different times $t/P_\star = 0, 0.15, 0.25, 0.33, 0.5$ and 1 . Fig. 10 (blue dashed line) shows the evolution of the average specific orbital energy of the

debris. The stream first crosses itself at $t/P_\star \simeq 0.15$ that is after the first passage of its leading part at pericentre (Fig. 11). When this occurs, most of the debris are still falling back towards the black hole away from the self-crossing point. It is different from model RI5e.8 for which this self-crossing happens later and when most of the debris are already beyond the self-crossing point. The reason for these differences is that the stream is longer for model RI5e.95 than for model RI5e.8. The debris located beyond the self-crossing point are expelled leaving the rest of the stream free to move around the black hole. It induces a second self-crossing which occurs at $t/P_\star \simeq 0.33$. These self-crossings of the stream create shocks which convert kinetic energy into thermal energy. This excess of thermal energy is radiated away instantaneously as a locally isothermal EOS is used. As a result, kinetic energy is effectively removed from the stream. The average specific orbital energy of the debris therefore decreases for $t/P_\star \gtrsim 0.15$ (Fig. 10). As a result, the debris move for their initial eccentric orbits to circular orbits (Fig.

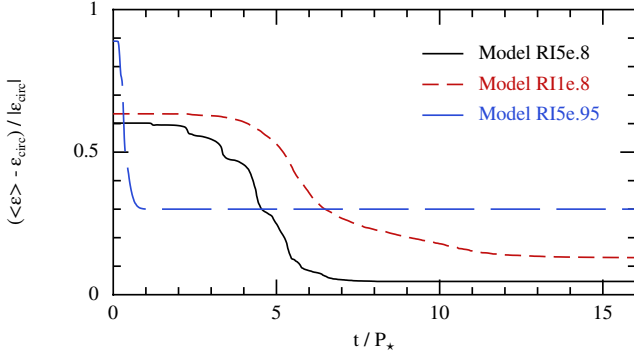


Figure 10. Evolution of the average specific orbital energy of the debris for models RI5e.8, RI1e.8 and RI5e.95. For these models, the periods of the star P_{\star} are respectively 2.8 h, 31 h and 22 h. The average specific orbital energy is shown relative to the specific circularization energy given by equation (17) for the relativistic potential.

11). At $t/P_{\star} \simeq 1$, the average specific orbital energy of the debris settles at value somewhat larger than the circularization energy (Fig. 10) and a thin and narrow ring of gas forms from the debris. It is located at a distance comparable to the circularization radius but somewhat larger (Fig. 11). These discrepancies with the specific circularization energy and the circularization radius are due to redistribution of angular momentum between the debris as for model RI5e.8.

For model RA5e.95, the debris evolve very similarly to model RA5.8. They expand due to shocks produced by the self-crossings of the stream. They settle into a thick and extended torus in which most of the debris are located between the circularization radius and the semi-major axis of the star. Only the value of these two limiting radii differs for the new orbit.

3.4 Convergence of the results

The simulations of the fallback phase has been performed for three different resolutions corresponding to about 100K, 500K and 1300K particles. The two larger resolutions have been obtained from the lowest one by using the particle splitting technique (Kitsionas 2003) on the initial condition of the fallback phase. Each particle is splitted into 5 or 13 additional ones with one at the position of the initial particle and the others distributed on a tetrahedron and on a face-centred cubic structure respectively. In both cases, the distance between each additional particles is fixed to 1.5 times the smoothing length of the initial one. In addition, the particles added outside the volume defined by the initial particles have been removed. The fraction of particles removed in this way is always less than 10%. The mass of the additional particles has then been decreased in order to keep the total mass of the stream constant.

Minor differences have been noticed when the resolution is increased. They are common to the different orbits considered. For a locally isothermal EOS, the time at which the average specific orbital energy of the debris settles is either advanced or delayed by $\Delta t \simeq P_{\star}$ between the 100K and the 500K simulations. However, this difference is suppressed between the 500K and 1300K simulations. Both for a locally isothermal and adiabatic EOS, increasing the resolution

also results in a smaller fraction of debris being accreted onto the black hole due to the decrease of their specific angular momentum. For the isothermal EOS, it causes the average specific orbital energy of the debris to settle at a value closer to the specific circularization energy. For an adiabatic EOS, it leads to a torus formed from the debris slightly more compact and centrally condensed. However, its internal structure remains the same. The simulations presented in this paper have been performed for 500K particles as both the final configuration of the debris and the time needed to reach it are unchanged above this resolution. Overall, we conclude that the behaviour described in the previous subsections is robust with respect to resolution.

4 DISCUSSION AND CONCLUSION

The light curve of TDE candidates is generally fitted by a $t^{-5/3}$ slope which traces the rate at which the stellar debris fall back towards the black hole. The underlying assumption is that the formation of an accretion disc from these debris occurs on a short timescale, after only a few orbits around the black hole. In this paper, we tested this assumption by means of SPH simulations for a star on a bound orbit. Our results confirm that circularization occurs on this timescale. It is driven by relativistic apsidal precession which causes the leading part of the stream to collide with the part that is still falling back towards the black hole. We also showed that the structure of the disc depends on the cooling efficiency of the gas by considering two extreme cases. For an efficient cooling, the debris form a thin and narrow ring of gas. For an inefficient cooling, they settle in a thick and extended torus mostly centrifugally supported against gravity. We also demonstrated the existence of different regimes of circularization for different orbits of the star. If the penetration factor is lower, relativistic apsidal precession is weaker and the circularization of the debris occurs more gradually. If the eccentricity of the star is larger, the stream is more extended when its leading part reaches the black hole. It causes the self-crossing of the stream to occur faster which accelerates the circularization.

Viscosity, not included explicitly in the simulations presented in this paper, could affect the evolution of the debris during the circularization process causing a fraction of the gas to be accreted onto the black hole. However, its influence can be estimated by computing the ratio of the viscous timescale t_{visc} to the circularization timescale t_{circ} . The value of t_{circ} for the different models is obtained from the simulations. It is parametrized by $n_{\text{circ}} = t_{\text{circ}}/P_{\star}$ which is roughly 1, 5 and 10 for models RI5e.95, RI5e.8 and RI1e.8 respectively (see Fig. 10). For the models using a locally isothermal EOS, the debris settle into a thin ring around the circularization radius. Evaluating t_{visc} at the circularization radius, the ratio is

$$\frac{t_{\text{visc}}}{t_{\text{circ}}} = 700 \left(\frac{n_{\text{circ}}}{5} \right)^{-1} \left(\frac{\alpha}{0.1} \right)^{-1} \left(\frac{H/R}{10^{-2}} \right)^{-2} \left(\frac{1-e^2}{0.36} \right)^{3/2}, \quad (18)$$

where α is the viscosity parameter (Shakura & Sunyaev 1973), H/R is the aspect ratio of the disc. The circularization radius is obtained from equation (14) which is at the origin of the $(1-e^2)^{3/2}$ factor. The above numerical

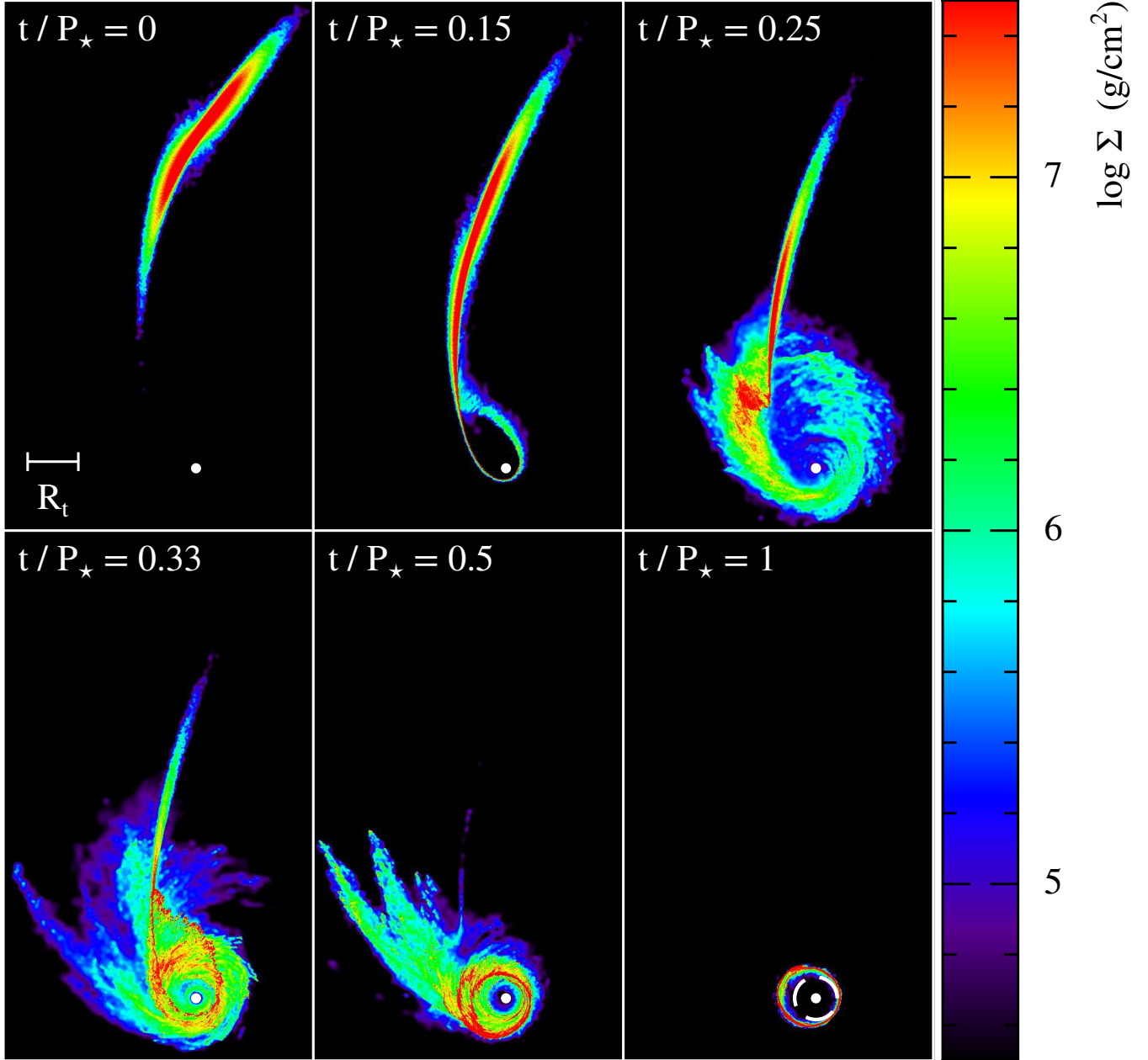


Figure 11. Snapshots of the fallback of the debris at different times $t/P_\star = 0, 0.15, 0.5$ and 1 for models RI5e.95. For this model, the period of the star P_\star is 22 h. The colours correspond to the column density Σ of the gas whose value is indicated on the colour bar. The white point represents the black hole. The dashed white circle on the last snapshot represents the circularization radius given by equation (15) for the relativistic potential. The stream is longer for this model than for model RI5e.8 as the eccentricity is larger. As a result, it self-crosses earlier and the debris move faster to circular orbits.

value corresponds to model RI5e.8. It only decreases slightly for models RI1e.8 and RI5e.95, to 300 and 500 respectively. Therefore, viscosity does not have a significant effect during the circularization of the debris and most of the accretion will occur during the subsequent evolution of the ring. An estimate of the accretion rate is given by $\dot{M} \simeq M_\star/t_{\text{visc}}$. It is $40\dot{M}_{\text{Edd}}$ for models RI5e.8 and RI5e.95 and $4\dot{M}_{\text{Edd}}$ for models RI1e.8, \dot{M}_{Edd} being the Eddington accretion rate assuming a radiative efficiency of 10%. Therefore, the debris are accreted at a super-Eddington rate. As a result, the thin ring will be puffed up by radiation pressure and form a

thicker and more extended structure. For the models using an adiabatic EOS, the debris settle in a thick torus located between the circularization radius and the semi-major axis of the star. Evaluating t_{visc} at the semi-major axis of the star, the ratio is

$$\frac{t_{\text{visc}}}{t_{\text{circ}}} = 0.3 \left(\frac{n_{\text{circ}}}{5} \right)^{-1} \left(\frac{\alpha}{0.1} \right)^{-1} \left(\frac{H/R}{1} \right)^{-2}. \quad (19)$$

It does not depend explicitly on the orbit of the star as P_\star cancels out. If t_{visc} is evaluated at the circularization radius, this ratio would be lower by a factor $(1 - e^2)^{3/2}$. As

previously, the above numerical value corresponds to model RI5e0.8. For models RI1e.8 and RI5e.95, it slightly varies to 0.1 and 1 respectively. It means that viscosity will affect the evolution of the debris driving the accretion of a fraction of them onto the black hole during the circularization process. The corresponding accretion rate $\dot{M} \simeq M_*/t_{\text{visc}}$ is $9 \times 10^4 \dot{M}_{\text{Edd}}$, $8 \times 10^3 \dot{M}_{\text{Edd}}$ and $10^4 \dot{M}_{\text{Edd}}$ for models RI5e0.8, RI1e.8 and RI5e.95 respectively. This highly super-Eddington accretion of the debris will cause the torus to become even thicker and more extended due to radiation pressure.

All the orbits considered for the star in this paper satisfy the condition $e < e_{\text{crit}}$ where e_{crit} is given by (2). In this regime, all the debris produced by the disruption stay bound to the black hole and are involved in the formation of the disc. As there is no subsequent fallback of debris towards the black hole, the mass accretion rate is not fixed by the fallback rate in this case. In subsection 3.3.2, the eccentricity of the star has been increased to $e = 0.95$ for $\beta = 5$. It causes the stream to self-cross after the first passage of its leading part at pericentre (see Fig. 11). As a result, the circularization timescale is $t_{\text{circ}} \simeq P_*$ that is $n_{\text{circ}} \simeq 1$. In general, the eccentricity above which this early self-crossing of the stream occurs is about 0.9 for both $\beta = 1$ and $\beta = 5$. Therefore, $n_{\text{circ}} \simeq 1$ for $e > 0.9$. If $e > e_{\text{crit}}$, debris continue to fallback towards the black hole after the circularization of the most bound ones. As $e_{\text{crit}} > 0.9$, $n_{\text{circ}} \simeq 1$ in this case. For a locally isothermal EOS, the condition $t_{\text{visc}} < t_{\text{circ}}$ is satisfied for $e > 0.9992 \simeq 1$ according to equation (18). Therefore, the debris are viscously accreted during their circularization only if the star is on a parabolic orbit. Otherwise, they circularize before being accreted and the mass accretion rate is not fixed by the fallback rate. For an adiabatic EOS, $t_{\text{visc}} \lesssim t_{\text{circ}}$ according to equation (19) which does not depend on the orbit of the star. In this case, the debris are viscously accreted during the circularization process and the mass accretion rate is fixed by the fallback rate. For a star on a parabolic orbit, the circularization process can then be predicted as follows. The stream self-crosses after the first passage of its leading part at pericentre. It leads to the rapid formation of a disc from the debris. These debris are viscously accreted while they circularize which is independent on the EOS, that is on the cooling efficiency of the gas. The inner radius of this disc is located at the circularization radius. Its structure approaches a thin and narrow ring if the gas cools efficiently and a thick and extended torus if the cooling is inefficient.

In the simulations presented in this paper, two extreme cooling efficiencies have been considered corresponding to a locally isothermal and an adiabatic EOS. The effect of cooling can be estimated a posteriori by computing the diffusion timescale t_{diff} defined as the time that photons take to diffuse out of the surrounding gas. As most of the thermal energy is produced by the shocks occurring when the stream self-crosses, the diffusion timescale must be evaluated at the location of these shocks. The gas being optically thick to electron scattering, it is given by $t_{\text{diff}} = H_{\text{sh}} \tau / c$ where $\tau = \sigma_{\text{T}} \rho_{\text{sh}} H_{\text{sh}} / m_{\text{p}}$ is the optical depth, H_{sh} and ρ_{sh} are the width and density of the gas at the location of the shocks. For the models using a locally isothermal EOS, the width of the gas remains $H_{\text{sh}} \simeq R_*$. To ensure the self-consistency of this model, the photons must diffuse out of the surrounding

gas before the circularization occurs. Therefore, the condition $t_{\text{diff}} < t_{\text{circ}}$ has to be satisfied which translates into an upper limit on the density

$$\rho_{\text{sh}} < 8 \times 10^{-7} \text{ g cm}^{-3} \left(\frac{n_{\text{circ}}}{5} \right) \left(\frac{H_{\text{sh}}}{R_*} \right)^{-2} \left(\frac{a_*}{100 R_{\odot}} \right)^{3/2}. \quad (20)$$

The above numerical value corresponds to model RI5e.8. For models RI1e.8 and RI5e.95, it is respectively $2 \times 10^{-5} \text{ g cm}^{-3}$ and $10^{-6} \text{ g cm}^{-3}$. The density of the gas is highly inhomogeneous at the time when most of the shocks occur. This condition is however satisfied for most of the gas for model RI1e.8 but not for model RI5e.8 and RI5e.95. Therefore, model RI1e.8 appears to be self-consistent. However, for models RI5e.8 and RI5e.95, the thermal energy created by the shocks is likely to affect the evolution of the gas during the formation of the ring. It would make it thicker and more extended similarly to models RA5e.8 and RA5e.95 which use an adiabatic EOS. However, these extrapolations are only approximate. The ability of radiation to escape depends on the precise location within the stream at which the thermal energy is deposited by the shocks. This radiation could also affect the structure of the disc through radiation pressure. A realistic treatment of thermodynamics is therefore necessary to determine precisely the effect of cooling during the circularization process.

The simulations presented in this paper are for a non-rotating black hole. If the black hole has a spin, the evolution of the debris should be qualitatively the same as described in this paper as long as the orbital plane of the star is aligned with the plane of the black hole. The only difference is a lower apsidal precession angle than for a non-rotating black hole. For a black hole spin $a = 0.9$, it decreases from 89.7 degrees to 50 degrees for $e = 0.8$ and $\beta = 5$, from 13.5 degrees to 11.5 degrees for $e = 0.8$ and $\beta = 1$ and from 80.7 degrees to 43.3 degrees for $e = 0.95$ and $\beta = 5$. Instead, if the orbital plane of the star is inclined with respect to the plane of the rotating black hole, the evolution of the debris could be qualitatively different. In this case, the debris experience nodal precession in addition to apsidal precession. Therefore, the orbital plane of the stream changes when it passes at pericentre. It could prevent the self-crossing of the stream and delay the circularization of the debris. The effect of the spin of the black on the circularization of the debris has been studied by Dai et al. (2013) but without considering the hydrodynamical interactions between the debris.

ACKNOWLEDGMENTS

We acknowledge the use of SPLASH (Price 2007) for generating the figures.

REFERENCES

- Amaro-Seoane P., Miller M. C., Kennedy G. F., 2012, MNRAS, 425, 2401
- Ayal S., Livio M., Piran T., 2000, ApJ, 545, 772
- Bate M. R., Bonnell I. A., Price N. M., 1995, MNRAS, 277, 362
- Cannizzo J. K., Gehrels N., 2009, ApJ, 700, 1047
- Cannizzo J. K., Troja E., Lodato G., 2011, ApJ, 742, 32

- Cappelluti N. et al., 2009, *A&A*, 495, L9
Chen X., Madau P., Sesana A., Liu F. K., 2009, *ApJL*, 697, L149
Chen X., Sesana A., Madau P., Liu F. K., 2011, *ApJ*, 729, 13
Coughlin E. R., Begelman M. C., 2014, *ApJ*, 781, 82
Dai L., Escala A., Coppi P., 2013, *ApJL*, 775, L9
Esquej P. et al., 2008, *A&A*, 489, 543
Evans C. R., Kochanek C. S., 1989, *ApJL*, 346, L13
Frank J., Rees M. J., 1976, *MNRAS*, 176, 633
Gezari S. et al., 2008, *ApJ*, 676, 944
Gezari S. et al., 2012, *Nat*, 485, 217
Gezari S. et al., 2009, *ApJ*, 698, 1367
Guillochon J., Manukian H., Ramirez-Ruiz E., 2014, *ApJ*, 783, 23
Guillochon J., Ramirez-Ruiz E., 2013, *ApJ*, 767, 25
Hayasaki K., Stone N., Loeb A., 2013, *MNRAS*, 434, 909
Kesden M., 2012, *Phys. Rev. D*, 86, 064026
Kitsionas S., 2003, PhD thesis, PhD Thesis, 2003
Kochanek C. S., 1994, *ApJ*, 436, 56
Komossa S., 2002, in *Reviews in Modern Astronomy*, Vol. 15, *Reviews in Modern Astronomy*, Schielicke R. E., ed., p. 27
Lacy J. H., Townes C. H., Hollenbach D. J., 1982, *ApJ*, 262, 120
Lodato G., King A. R., Pringle J. E., 2009, *MNRAS*, 392, 332
Lodato G., Price D. J., 2010, *MNRAS*, 405, 1212
Lodato G., Rossi E. M., 2011, *MNRAS*, 410, 359
Loeb A., Ulmer A., 1997, *ApJ*, 489, 573
Morris J., Monaghan J., 1997, *Journal of Computational Physics*, 136, 41
Phinney E. S., 1989, in *IAU Symposium*, Vol. 136, *The Center of the Galaxy*, Morris M., ed., p. 543
Price D. J., 2007, *PASA*, 24, 159
Price D. J., Federrath C., 2010, *MNRAS*, 406, 1659
Ramirez-Ruiz E., Rosswog S., 2009, *ApJL*, 697, L77
Rees M. J., 1988, *Nat*, 333, 523
Seto N., Muto T., 2010, *Phys. Rev. D*, 81, 103004
Shakura N. I., Sunyaev R. A., 1973, *A&A*, 24, 337
Shen R.-F., Matzner C. D., 2014, *ApJ*, 784, 87
Stone N., Loeb A., 2011, *MNRAS*, 412, 75
Strubbe L. E., Quataert E., 2009, *MNRAS*, 400, 2070
Tejeda E., Rosswog S., 2013, *MNRAS*, 433, 1930
van Velzen S. et al., 2011, *ApJ*, 741, 73